

Ground Plane-Aided Extrinsic Calibration of Inertial and RGB-D Sensors for Uncrewed Aerial Vehicles

Ilyar Asl Sabbaghian Hokmabadi* and Mahdis Bisheban †
University of Calgary, Calgary, Alberta, AB T2L 1Y6

Accurate extrinsic calibration of inertial sensors, such as Inertial Measurement Units (IMUs) and cameras is crucial for trajectory estimation of Uncrewed Aerial Vehicles (UAVs). While numerous calibration methods have been proposed, these techniques often rely on specialized equipment, planar targets, and an initial estimate of the calibration parameters. In this research, we propose a targetless calibration method designed for UAVs equipped with IMUs and RGB-Depth (RGB-D) cameras. Our approach leverages deep-learning-based floor-segmentation to extract ground points from the depth channel of RGB-D images. Subsequently, the normal vector to these points is estimated. The known orientation of the normal to the floor segment and the gravity vector sensed in the accelerometer's frame are utilized in a robust estimation approach to estimate the extrinsic calibration parameters. We illustrate that the developed method outperforms MATLAB's Toolboxes and exhibits similar performance to Kalibr without the use of specialized checkerboard targets.

I. Introduction

Sensor fusion between Inertial Measurement Units (IMUs) and cameras is critical for autonomous systems. This fusion has been widely used to estimate the attitude, position, and velocity of Uncrewed Aerial Vehicles (UAVs) [1]. However, accurate path and trajectory estimation depends on the precise determination of extrinsic calibration parameters, which are defined as the translation and rotation between the coordinate frames of the sensors.

Extrinsic calibration methods can be categorized into target-based and targetless approaches. Target-based methods [2, 3] rely on specialized equipment such as checkerboards. A key limitation of these methods is the need to maintain visibility of the calibration target, which is particularly challenging in UAV applications. Target-less calibration methods [4–7] rely on online trajectory estimation. However, this approach can be unreliable due to the need for the availability of visual features, which depend on environmental texture and lighting conditions. This can be challenging as camera-based trajectory estimation relies on salient point detection and matching in consecutive images. Such salient points can only be detected if there are objects in the environment with visual textures, under suitable illumination conditions. Moreover, low-cost IMU-based trajectory estimation can also be challenging due to error accumulation. Therefore, it is important to develop calibration methods that do not depend on salient feature point detection and special visual targets. Further, such calibration should be independent of the trajectory estimation of a UAV unlike the methods proposed in [8, 9].

The initialization problem for extrinsic calibration parameters is crucial and recognized as challenging [10]. In [10], the authors address this initialization problem by first estimating the relative orientation between two camera frames at consecutive epochs using Nistér's five-point algorithm [11]. The relative orientation of the IMU between two frames captured at two consecutive epochs in the trajectory is also estimated using gyroscope measurements. The initial extrinsic calibration is then obtained by minimizing the error between these two relative rotations. However, this approach still relies on two consecutive frames. [12] proposes a coarse initialization method for LiDAR–IMU calibration. Their method requires a sloped surface to estimate the relative extrinsic orientation between the IMU and the LiDAR. This approach is similar to [10] in that it also requires estimating the relative motion between the two frames. In contrast, the method proposed in this paper utilizes corresponding accelerometer–RGB-D measurement directly, without relying on two-view relative motion estimation, therefore, reducing the computational cost of the algorithm.

These limitations highlight the need for calibration methods that do not rely on artificial targets or continuous trajectory estimation. Our research addresses this gap by proposing a robust, targetless calibration approach that is

*Postdoctoral Associate, Department of Mechanical and Manufacturing Engineering, 40 Research PI NW, Calgary

†Assistant Professor, Department of Mechanical and Manufacturing Engineering, 40 Research PI NW, Calgary, AIAA Member. This work was supported by the Natural Sciences and Engineering Research Council of Canada (NSERC), the Government of Alberta, Alberta Innovates, and the Schulich School of Engineering at the University of Calgary. Funding was awarded to Dr. Mahdis Bisheban, Director of the Intelligent Dynamics and Control Lab and Assistant Professor at the University of Calgary.

independent of trajectory estimation and better suited for UAV operations. In our method, the floor normal vector is assumed to be parallel to the gravity vector, which is a reasonable assumption in structured, indoor environments. By aligning the estimated floor normal vector with the gravity vector measured in the accelerometers' coordinate frame, the relative orientation between the IMU and RGB-D camera can be inferred. While the proposed method relies on the visibility of the ground segment in RGB-D images, this is a reasonable assumption in most indoor, human-made environments, where flat floors are typically unobstructed. Unlike traditional feature-based methods that depend on textured objects or rich visual scenes, our approach leverages the structural regularity of indoor floors, which are consistently present and detectable even under varying lighting conditions. Unlike methods [2] that require continuous feature detection, the proposed calibration approach uses discrete pairs of IMU measurements and RGB-D images containing visible ground plane segments to estimate the extrinsic parameters.

Ground plane detection plays a key role in many land-based robotic applications. For land vehicles with a fixed monocular camera height relative to the ground, the scale ambiguity of visual features on the ground is immediately resolved using the available height information. Ground plane detection helps identify these important features and assigns 3D coordinates to them [13], without requiring feature matching and multi-frame triangulation, and ultimately improves camera trajectory estimation [14]. Ground plane detection is also important in imposing height constraint on LiDAR/camera during the trajectory estimation of wheeled vehicles. This height constraint is crucial for the ubiquitous LiDAR-based odometry. LiDAR height obtained from LiDAR odometry is often not restricted to a direction parallel to the ground. This is due to the fact that features such as trees or street poles do not provide a strong vertical constraint. This will lead to error accumulation in the vertical (to the ground plane) direction. In order to address this challenge, ground-plane detection is utilized to identify features lying on this plane and help constraining the estimated height of the trajectory [15]. In [16] ground plane detection is utilized to constrain the height estimate of a mobile wheeled robot, as well as to estimate the extrinsic calibration parameters of the LiDAR and IMU. [17] utilized ground-plane height constraint similar to [16] and improved the accuracy further by utilizing map matching between the current LiDAR point cloud and the available pre-processed point cloud of the environment. Ground-plane detection has also been utilized for RGB-D-based motion estimation of mobile wheeled robots in [18].

Ground-plane detection plays a key role in the navigation and control of a UAV, as well. [19] uses a downward-looking rangefinder to detect the ground and estimate the height of a UAV in the indoor environment. However, since a UAV can hover over objects above the ground, such height estimation is prone to errors. [20] proposes a method to estimate the ground plane in order to estimate the constant height of a UAV in a cluttered under-canopy environment. More recently, in [21], ground plane detection has been employed to allow for the reduction of the dimensionality of 3D pose estimation to 2D and improve the computational cost of particle filtering. Their method reduces the particle sampling space dimensions by first estimating the height of the UAV from the ground. The estimated height restricts particle filter sampling of the position from 3D to a 2D plane. Ground-plane detection is also useful in emergency landing for UAVs. [22] proposes a deep learning based image segmentation method to identify the largest empty space on the ground for a UAV to land in an emergency landing situation.

Because of the importance of ground/floor detection, many researchers have focused on improving its accuracy. In [23], a ground/floor segmentation approach is proposed using two cameras. A downward-looking RGB-D camera is utilized to initiate the seeds for a region-growing algorithm. The corresponding pixels in a fish-eye camera (the second camera) are found and expanded to detect the entire floor segmentation. This approach assumes the availability of a downward-looking RGB-D camera. The authors in [24] detect the ground plane by first estimating the trajectory of the monocular camera. The estimated trajectory and the corresponding identified features in the images are triangulated. Subsequently, the normal to each point is extracted by fitting local planes. They assumed that the ground plane normal is orthogonal to the direction of the camera's motion throughout the vehicle's trajectory, which is not an assumption made in our proposed method. Ground plane detection can be facilitated by using sensors with rich 3D information, like 3D LiDARs. A survey of LiDAR-based ground plane detection [25] shows that this plane can be estimated using LiDAR data. This is especially true for ground vehicles and mobile wheeled robots, as typically, the approximated height of the LiDAR from the ground is known. In [26], the authors propose to cluster LiDAR points into height intervals. This limits the search for the ground plane to a certain interval, reducing the computational cost. However, relying on the assumption of constant sensor height is not applicable in many UAV-based applications. Further, LiDARs are more expensive and heavier, making them less suitable for low payload UAV missions compared to RGB-D cameras. The proposed method achieves floor-segmentation with the help of the RGB channel, instead.

Classical methods, introduced above, do not rely on data-driven, learning-based algorithms for ground detection and segmentation. They are not robust because ground and specifically indoor floor planes are often made of reflective material, which produces unpredictable features for classical hand-crafted feature-detection approaches such as Scale

Invariant Feature Transform (SIFT) [27], thereby limiting the broader applicability of these methods. More recently, learning-based methods have been explored for floor and ground segmentation [28]. In [28], a deep-learning-based approach for ground plane segmentation and surface-normal detection is proposed; however, their method is primarily tested on road segments. Similarly, [29] proposed a fully convolutional neural network (FCN)-based approach comparable to the method presented in this paper. However, their model is trained for outdoor ground detection, such as garden beds, whereas the proposed method is trained for indoor environments. In [30], the ground plane is detected by first projecting the 3D point cloud onto a 2D image-like grid, where point height is encoded in the feature channel, and a neural network is trained on these 2D representations for ground segmentation. The proposed method of this paper does not require the depth channel for ground detection and relies only on the RGB information.

Floor-normal detection is an important step in the proposed extrinsic calibration method. The normal of the floor plane is obtained after floor segmentation. In particular, the depth values of pixels belonging to the floor segment can be used to estimate the floor-plane normal. Since RGB-D measurements are contaminated with noise, robust plane-fitting methods are required. Plane fitting to noisy point clouds can be achieved using methods such as the Hough transform, originally introduced in [31]. Hough transformation is a histogram-voting algorithm in which a stencil of lines passing through each point is parameterized by orientation and distance to the origin. Votes are then added to the corresponding bins for each point. The bin with the highest number of votes is selected as the solution. The Hough transform is computationally feasible in 2D because the histogram involves only two parameters; however, extending it to 3D plane fitting increases the dimensionality, which significantly increases computational complexity. This high computational cost in higher-dimensional spaces is examined in [32]. Another method for robust plane fitting is DBSCAN [33], a point cloud density-based clustering algorithm. Its robustness makes it suitable for rejecting outlier points before fitting a plane to the inliers. DBSCAN classifies data points into three groups: core, reachable, and noise points. Core points have a minimum number of neighboring points within a specified radius. Reachable points lie within this radius of a core point. Points that do not satisfy either condition are labeled as noise. DBSCAN requires tuning of two hyperparameters. RANSAC is another robust plane-fitting technique that removes outliers during estimation. Many variants of RANSAC have been introduced since its inception [34], and RANSAC has been used for plane fitting [35]. Like DBSCAN, RANSAC requires hyperparameter tuning. Finally, Singular Value Decomposition (SVD) can also be used to fit a plane. SVD is a computationally efficient method and is used for datasets containing relatively few outliers. Due to the high accuracy of the floor segmentation in our pipeline, we rely on SVD for floor-plane fitting to reduce computational cost.

We summarize the contributions of this work as follows: (1) A targetless extrinsic calibration method for an RGB-D camera and IMU is proposed. The developed method leverages semantic segmentation to extract the floor segment from RGB-D camera images. The normal of this plane and the gravity vector from the IMU are used to estimate the extrinsic calibration parameters. (2) The proposed method does not require an initialization of the extrinsic calibration parameters. (3) The developed method is a general-purpose extrinsic calibration approach for an IMU and RGB-D camera and can be used on both land and aerial robots. No assumption about a fixed RGB-D camera relative to the ground plane is made. (4) We further demonstrate the importance of intrinsic IMU calibration for achieving more accurate extrinsic calibration.

II. Methodology

The developed extrinsic calibration approach consists of three modules. The first two modules perform RGB-D image processing and accelerometer processing, explained in Section II.A and II.B, respectively. The detected floor normal and the gravity vector are then matched to estimate the extrinsic orientation parameters, explained in Section II.C. An overview of the proposed method is shown in Fig. 1.

A. Module 1: RGB-D Image Processing

The first module includes five steps: pinhole camera calibration, RGB to depth channel calibration, floor segmentation, depth channel pixel back-projection, and floor plane normal detection.

Pinhole camera calibration (Module 1, Step 1) includes estimation of the location of the orthogonal projection of the optical center of the camera onto the image plane. This projection is often close to the center of the image and is denoted with two coordinates as $c_x \in \mathbb{R}$ and $c_y \in \mathbb{R}$. Pinhole camera calibration also includes the focal length, which is the distance from the optical center to the image-forming plane. The focal lengths in the x and y axes ($f_x \in \mathbb{R}$, $f_y \in \mathbb{R}$) are considered separate parameters. The fifth pinhole camera calibration parameter is the skew parameter $\gamma \in \mathbb{R}$. In total, pinhole camera calibration includes five parameters ($f_x, f_y, c_x, c_y, \gamma$). For most cameras, these parameters are only required to be estimated once. The pinhole camera calibration matrix is shown in Equation (1), where \bar{u} and \bar{v}

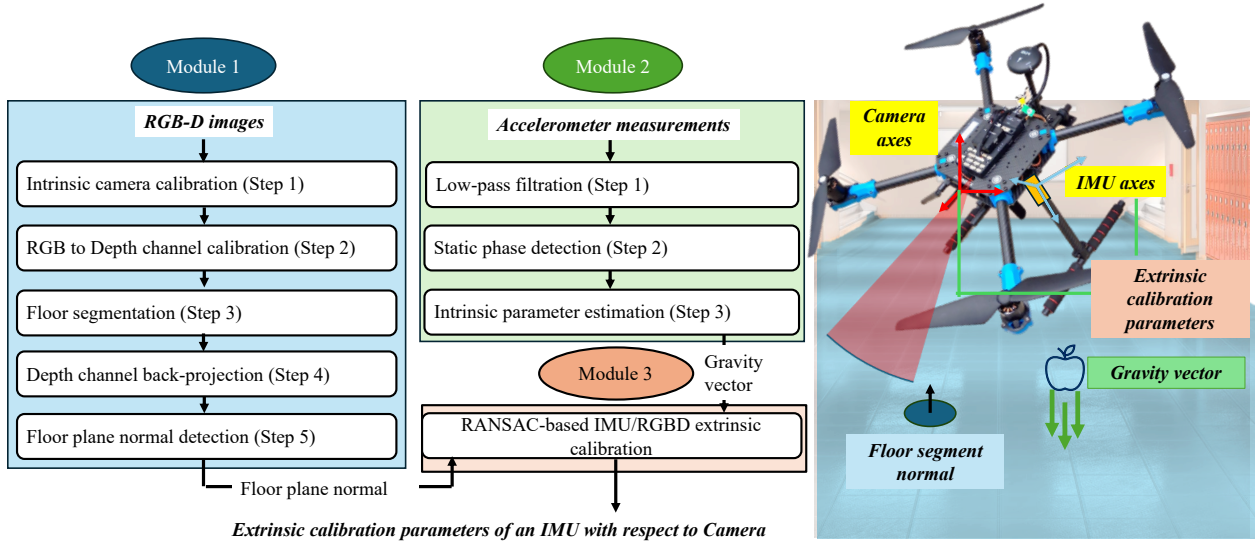


Fig. 1 The proposed extrinsic calibration of an IMU and an RGB-D camera for UAV-based trajectory estimation

denote the normalized coordinates of the pixels and u and v are the pixels in the image frame.

$$\begin{bmatrix} u \\ v \\ 1 \end{bmatrix} = \begin{bmatrix} f_x & \gamma & c_x \\ 0 & f_y & c_y \\ 0 & 0 & 1 \end{bmatrix} \begin{bmatrix} \bar{u} \\ \bar{v} \\ 1 \end{bmatrix}. \quad (1)$$

Pinhole camera calibration parameters cannot capture non-linear distortions. Such non-linear distortions can cause straight lines to appear curved in images. The non-linear distortions are typically included in the intrinsic camera calibration process as well. The most significant non-linear distortion is known as radial distortion, which happens due to the opening and closing of the camera shutter. Assuming that the distorted normalized coordinates of the pixels are denoted as \bar{u}_{dist} and \bar{v}_{dist} , and radial distortion coefficients are denoted as λ_1 , λ_2 , and λ_3 , radial distortion equations are shown in the following [36],

$$\begin{aligned} \bar{u}_{dist} &= \bar{u} \left(1 + \lambda_1 r^2 + \lambda_2 r^4 + \lambda_3 r^6 \right), \\ \bar{v}_{dist} &= \bar{v} \left(1 + \lambda_1 r^2 + \lambda_2 r^4 + \lambda_3 r^6 \right), \end{aligned} \quad (2)$$

where $r^2 = \bar{u}^2 + \bar{v}^2$. In our experiments, we have used MATLAB™ Camera Calibration Toolbox [37] and a checkerboard in an offline process to estimate these parameters.

Followed by the intrinsic camera calibration, the unknown translation and the orientation of the depth channel, the camera should be estimated (Module 1, step 2). This step ensures that there is a correct alignment between the pixels in the depth channel and the pixels in the RGB channel. These parameter (which includes a rotation $R_{RGB}^D \in SO(3)$ and the translation vector $T_{RGB}^D \in \mathbb{R}^3$) are provided by the manufacturer.

In Module 1, Step 3, the images obtained from the RGB channels of the camera are utilized to segment the floor region. In this work, in order to ensure that floor segmentation is achieved with high accuracy, a deep neural network is trained to segment the floor in RGB images. Once RGB-based floor segmentation is achieved, the corresponding pixel depth can be extracted from the depth (D) channel. The deep neural network utilized for this training is a fully convolutional neural network (FCN), which has an encoder-decoder architecture described. The input size to this neural network is equal to height (H) and width (W) of the images. The output is a binary image with the same height and width as the input image. The corresponding pixels to the floor segment are labeled as binary high (one), and the other pixels are labeled as binary low (zero). The trained neural network has four encoder and decoder layers. The input to this network is an image of 256 by 256 RGB pixels. The convolutional kernel size is 2 by 2 with a kernel stride of 2. The network includes 31,031,745 parameters in total, and it is trained using approximately 100,000 images. The

database includes the flipping, rotation, contrast variation, and blurring data augmentations. The loss function is defined as the binary cross-entropy. Adam’s optimizer with an initial learning rate of 0.001 with a batch size of 16 is utilized. The output of a binary segmentation algorithm requires a threshold to identify the foreground pixels (the floor segment) from the background pixels. In our experiments, this value is 0.5 (the value range of the output pixels is between 0 to 1).

In Step 4, the depth values corresponding to the segmented floor pixels are back-projected using the camera intrinsic matrix to generate a 3D point cloud $(x, y, z) \in R^3$ in the camera coordinate frame, where each point represents a physical location on the floor surface. In order to back-project these pixels, the pinhole camera model (outcome of Module 1, Step 1), and the RGB to depth channel calibration (outcome of Module 1, Step 3) are required. With these, the following back-projection equation can be utilized

$$\begin{bmatrix} x \\ y \\ z \end{bmatrix} = Z \begin{bmatrix} \frac{1}{f_x} & -\frac{\gamma}{f_x f_y} & \frac{\gamma c_y - c_x f_y}{f_x f_y} \\ 0 & \frac{1}{f_y} & -\frac{c_y}{f_y} \\ 0 & 0 & 1 \end{bmatrix} \begin{bmatrix} u^F \\ v^F \\ 1 \end{bmatrix}, \quad (3)$$

where $Z \in \mathbb{R}$ is the normalized $([0, 1])$ gray-scale pixel value of the depth channel, and u^F and v^F are the coordinates of the pixels residing on the floor-segment. It is important to note that a global scale to transform the back-projected pixels to metric scale is required. This scale is constant for all the pixels, and for an RGB-D camera, it is often provided by the manufacturer.

Next, in Module 1, Step 5, the floor plane normal is detected. In most environments, particularly indoor spaces, the floor segment corresponds to a set of co-planar points that lie on a common plane. These points, extracted from the depth channel of an RGB-D image, represent the visible portion of the floor surface. However, depending on the environment, the co-planarity assumption might not always hold. The normal vector to the segmented plane can be estimated using well-known plane fitting algorithms (Module 1, Step 4). In the proposed method, Singular Value Decomposition (SVD) is utilized to estimate a best-fit normal vector to these points. SVD algorithm outputs singular vectors. These vectors are ordered such that the first component corresponds to the direction with the largest variance, and the last component corresponds to the direction with the smallest variation in the data. Since points corresponding to a planner surface are expected to vary the least in the direction perpendicular to the plane, the vector corresponding to the smallest singular value is considered as the plane normal. In order to show the derivation of the floor normal in the camera frame, mathematically, we commence by stacking the homogeneous coordinate points of the point cloud in a matrix $P_k \in \mathbb{R}^{m \times 4}$ shown in the following, where m and k are the number of points and the number of current epoch, respectively.

$$P_k = \begin{bmatrix} x_1 & y_1 & z_1 & 1 \\ x_2 & y_2 & z_2 & 1 \\ \vdots & \vdots & \vdots & \vdots \\ x_m & y_m & z_m & 1 \end{bmatrix}. \quad (4)$$

The SVD algorithm decomposes the matrix $P_k = U D V^T$ to three matrices $U \in \mathbb{R}^{3 \times 3}$, $D \in \mathbb{R}^{3 \times 3}$ and $V \in \mathbb{R}^{3 \times 3}$, where U and V are orthonormal matrices. D is diagonal with positive real values. With the help of SVD, the smallest eigen vector ($V(:, 4)$) can be selected. This eigen vector corresponds to the floor normal of the point cloud, and it is shown in the following,

$$V(:, 4) = \begin{bmatrix} d_1 \\ d_2 \\ d_3 \\ d_4 \end{bmatrix}, \quad \text{with the plane equation defined as } d_1 x + d_2 y + d_3 z + d_4 = 0. \quad (5)$$

Finally, the plane normal $v_k^C \in \mathbb{R}^3$, which is required in Module 3, can be calculated by normalizing the $V(:, 4)$ using the homogeneous part of the vector in the following, where the superscript c denotes the current camera frame,

$$v_k^C = \frac{1}{\sqrt{d_1^2 + d_2^2 + d_3^2}} \begin{bmatrix} d_1 \\ d_2 \\ d_3 \end{bmatrix}. \quad (6)$$

B. Module 2: Accelerometer Processing

Module 2 includes three steps. Low-pass filtering of accelerometer measurements, static phase detection, and estimation of intrinsic parameters. The output of this module is an estimated of the gravity vector. Low-pass filtering (Module 2, Step 1) is the first step that ensures the removal of high-frequency components of the signal’s spectrum. In the experiments, Butterworth filtering is utilized with a cut-off frequency of f_c and an order of L . The frequency filtering is applied to each axis of accelerometer data independently.

Followed by this low-pass filtering, in Step 2, the static phases are detected using the magnitude of the accelerometer data. A static phase is an interval where the magnitude of change in the accelerometer’s data is smaller than a certain threshold. Such a threshold is sensor dependent, and in this work, the value is set to $0.01 (m/s^2)$. Further, a minimum window size is used to reject false data in the static phase detection. The size of this window depends on the time the sensor is kept in static phases. In our experiment, the window size corresponds to approximately 0.5 seconds. The importance of utilizing the static phase detection is due to the fact that intrinsic accelerometer calibration (Module 2, Step 3) relies on known measurements of the gravity vector’s magnitude. The magnitude of the accelerometer readings can only be assumed to be equal to gravity when no other external forces are applied to this sensor. These phases here are denoted as static phases.

In Step 3, the intrinsic calibration of accelerometers is estimated. This step is important to track the direction of gravity accurately using accelerometers. Intrinsic calibration helps mitigate the errors between the expected and the actual outputs of an IMU. These parameters are independent of how the IMU is mounted on the UAV. For a triaxial accelerometer, these calibration parameters can be summarized as scale ($s \in \mathbb{R}^3$), bias ($\mathbf{b} \in \mathbb{R}^3$), and non-orthogonality ($\mathbf{n} \in \mathbb{R}^3$). The bias is defined as an offset from the zero measurements when no external forces are applied to the sensor (the accelerations are zero). The scale factor is the ratio of the true and the actual outputs of the sensor. Non-orthogonality captures any projection of the three axes of a triaxial accelerometer on other axes. Ideally, for a sensor, these axes should be mutually orthogonal with non-orthogonal values of zero.

In order to calibrate the accelerometer, the method in [38, 39] is utilized. This approach requires a UAV or the device to be placed at different static phases. Static phases are utilized to estimate all the unknown linear calibration parameters of an accelerometer (Step 3). These calibrated accelerometers measure the gravity vector in the sensor’s body frame, which can be used directly in the estimation of the extrinsic calibration as it will be explained in Section II.C. This process does not require gyroscopes. This is an important advantage as gyroscope measurements can suffer from g-dependent bias variations [40] and, in general, bias instability [41], making its calibration challenging. Further, utilizing this approach, instruments such as a triaxial turntable are not required; thus rendering the proposed approach suitable for in-suite calibration. The calibration model used for an accelerometer (Module 2, Step 3) is shown in the following:

$$\mathbf{a}_k^B = M\tilde{\mathbf{a}}_k^B + \mathbf{b}_k + \boldsymbol{\eta}, \quad \boldsymbol{\eta} \sim \mathcal{N}(0, \Sigma). \quad (7)$$

where $\tilde{\mathbf{a}} \in \mathbb{R}^3$ denotes uncalibrated and filtered accelerometer measurements, while $\mathbf{a} \in \mathbb{R}^3$ refers to the calibrated and filtered accelerometer measurements. Random errors in the measurements are modeled as a Gaussian distribution shown as ($\boldsymbol{\eta} \in \mathbb{R}^3$) with the covariance matrix shown as $\Sigma \in \mathbb{R}^{3 \times 3}$. The superscript B indicates that the measurements are obtained in the sensor body frame. These measurements are utilized to estimate the unknown orientation of the camera with respect to the body frame. The calibration matrix $M \in \mathbb{R}^{3 \times 3}$ includes axes non-orthogonality ($\mathbf{n} = [n_{xy}, n_{xz}, n_{yz}]$), and the scale factor ($\mathbf{s} = [s_x, s_y, s_z]$) as follows

$$M = \begin{bmatrix} s_x & n_{xy} & n_{xz} \\ 0 & s_y & n_{yz} \\ 0 & 0 & s_z \end{bmatrix}. \quad (8)$$

C. Module 3: RGBD/IMU Extrinsic Calibration

Module 3 is the proposed Ground-plane based RANdom SAMple Consensus (RANSAC) IMU/RGB-D extrinsic calibration, where unknown extrinsic calibration parameters of the camera and the IMU are estimated by aligning the floor-normal vector and gravity vector over K samples. The unknown extrinsic calibration parameters of the camera and the IMU are shown by $R_B^C \in SO(3)$. The K samples are gathered over specific trajectories. During these trajectories, IMUs should experience different poses with respect to the gravity vector. This ensures that the extrinsic calibration can be achieved successfully. Specifically, the device (with IMU and camera) should experience rotations around three perpendicular axes.

In Module 3, the proposed method estimates a rotation matrix (corresponding to the unknown extrinsic orientation) that can minimize the total error between the gravity vector in the IMU and RGB-D frames as shown in the following,

$$e = \frac{1}{2} \sum_k w_k \|\mathbf{v}_k^C - R_B^C \mathbf{a}_k^B\|^2, \quad (9)$$

where $\mathbf{v}_k^C \in \mathbb{R}^3$ is the floor-plane normal in the RGB-D camera frame, $\mathbf{a}_k^B \in \mathbb{R}^3$ is the calibrated acceleration in the static phase in IMU frame, which roughly corresponds to the gravity vector if the sensor is static or it is not moved too fast. The filtering of the accelerometer introduced in the previous section helps remove high-frequency vibrations from the data. The unknown $R_B^C \in SO(3)$ is the extrinsic calibration matrix, which $w_k \in \mathbb{R}^K$ is a weight coefficient. Equation (9) is known as Wahba's problem [42]. There are numerous approaches proposed to address this problem [43, 44]. In this paper, we propose a RANSAC-based solution. First, we reformulate Equation (9) as a standard least squares estimation. In order to achieve this, we commence from the following,

$$\mathbf{v}_k^C = R_B^C \mathbf{a}_k^B. \quad (10)$$

We can rewrite Equation (10) in terms of 9 unknown parameters of the rotation matrix as shown in the following,

$$\mathbf{v}_k^C = \begin{bmatrix} x a_k & y a_k & z a_k & \mathbf{0}_{1 \times 3} & \mathbf{0}_{1 \times 3} \\ \mathbf{0}_{1 \times 3} & x a_k & y a_k & z a_k & \mathbf{0}_{1 \times 3} \\ \mathbf{0}_{1 \times 3} & \mathbf{0}_{1 \times 3} & x a_k & y a_k & z a_k \end{bmatrix} \mathbf{r}, \quad (11)$$

where the bold symbol $\mathbf{r} \in \mathbb{R}^9$ indicates vectorized nine unknown parameters of the extrinsic rotation matrix. The three equations shown above represent one measurement correspondence at a time k . The left-hand side and the matrix rows can be stacked as for $k \in [1, K]$, as shown in the following

$$\mathbf{v}_{1:K}^C = A \mathbf{r}. \quad (12)$$

The solution to this standard least square form is shown in the following

$$\mathbf{r} = (A^T W^{-1} A)^{-1} W^{-1} A^T \mathbf{v}_{1:K}^C, \quad (13)$$

where $W \in \mathbb{R}^{3K \times 3K}$ is the weight of the measurements (similar to the Wahba's formulation).

The estimated rotation parameters between an IMU and a camera can be reorganized into a matrix form, $\tilde{R}_B^C \in \mathbb{R}^{3 \times 3}$. In addition, the orthogonality constraint can be imposed using SVD. The estimated rotation parameters can be reorganized into a matrix form (\tilde{R}_B^C), then we can compute the SVD of this matrix as $\tilde{R}_B^C = U D V^T$. Finally, multiplying U and V^T will result in a corrected rotation matrix R_B^C , as shown in

$$R_B^C = U V^T. \quad (14)$$

To validate the proper rotation, we ensure the determinant is +1 and $R^T R = I$.

Removing outliers is an important step, as some of the floor-normal and gravity measurements in the data can have errors that cannot be mitigated relying only on the least square-based technique shown above. Such robustness can be achieved by randomly sampling from the measurements to find an inlier set. The proposed method requires three measurement pairs. Each measurement pair provides three equations, and there are in total of nine equations to estimate the unknowns. Once the extrinsic calibration parameters are estimated, they are tested using residual errors of the other measurements. Outliers are defined as those measurements with residual error larger than a user-defined threshold τ . RANSAC stops when an extrinsic calibration with a sufficiently large inlier-to-outlier ratio is found. The pseudo code of the developed RANSAC-based robust estimation is shown in Algorithm 1.

III. Results and Discussion

To validate the developed method, low-cost sensors are used. These sensors are mounted on a platform as shown in Fig. 2. The sensors are connected to an onboard computer where the incoming measurements are time-synchronized. Specifically, we used the Gemini 2 RGB-D camera by Orbbec™ [45]. This RGB-D camera is equipped with one stereo pair and an IR distance sensor. This camera measures the distance at a range of 0.25 to 2.5 meters with a horizontal field

Algorithm 1 RANSAC [34] for Extrinsic Calibration using Floor Normals and Gravity Vectors

Require: Floor normals from RGB-D camera \mathbf{v}_k^c , gravity vectors from IMU \mathbf{a}_k^B , threshold τ

Ensure: Estimated rotation matrix R_c^B

```
1: Initialize: Inlier threshold  $\tau$ , best rotation  $R_c^B \leftarrow I$ 
2: while  $\alpha > \tau$  do
3:   Randomly select a minimal subset of correspondences:  $(\mathbf{v}_k^c, \mathbf{a}_k^B)$ 
4:   Estimate rotation  $R_c^B$  using (13)-(14)
5:   Initialize inlier count  $\alpha \leftarrow 0$ 
6:   for Remaining pairs of  $\mathbf{v}_k^c, \mathbf{a}_k^B$  do
7:     Compute error :  $\|\mathbf{a}_k^B - R_c^B \mathbf{v}_k^c\|$ 
8:     if error  $< \tau$  then
9:        $\alpha \leftarrow \alpha + 1$ 
10:    end if
11:  end for
12: end while
13: return  $R_c^B$ 
```

of view of 67.9° and a vertical field of view of 45.3° . The depth accuracy of the sensor at 1 meter is approximately 5 millimeters. This camera outputs RGB and depth. The depth channel is aligned to one of the stereo cameras using the manufacturer's calibration parameters. For this research, images of 640×480 pixels are utilized. The camera frame rate is set to $5Hz$.

Three IMUs, ISM330DHCX [46], LSM6DSOX [47] by STMTM, and MPU6050 [48] by TDKTM, are used in the tests. Expansion electrical boards are designed by Adafruit Industries LLCTM for these IMUs. The IMUs are from different generations to ensure the applicability of the developed calibration method across different generations of MEMS IMUs. MPU6050 is from an older generation of sensors. LSM and ISM series belong to the newer generation. The input data rate for these IMUs was set to $60Hz$. The input data rate for MPU6050 was set to $80Hz$.

The camera intrinsic calibration parameters of Module 1, Step 1 are reported in Table 1. In total, 19 images are used to estimate these parameters. The mean reprojection error achieved is sub-pixel. This indicates a high quality of calibration. Besides the pinhole camera model, radial distortion was found in the image as well. The estimated radial distortions $(\lambda_1, \lambda_2, \lambda_3)$ are also reported in Table 1. RGB to depth calibration parameters in Module 1, Step 2 (R_{RGB}^D and T_{RGB}^D) are provided by the manufacturers.

In Module 1, Step 3, The developed floor-segmentation method is tested using two datasets. The first dataset is collected in an indoor environment similar to the training set. The second dataset is collected from online databases. In order to collect these images, the keywords "hospital corridor", "office corridor", and "airport corridor" are used in a Google search. From the recommended images by this search engine, 33 images are selected. In selecting the images, a user judges the similarity of the images to the training set and selects more similar images. Some examples of the images and segmented floor are shown in 3. In order to illustrate the performance of the trained network quantitatively, the mean and standard deviation of the precision and recall values are calculated. These quantities are defined as

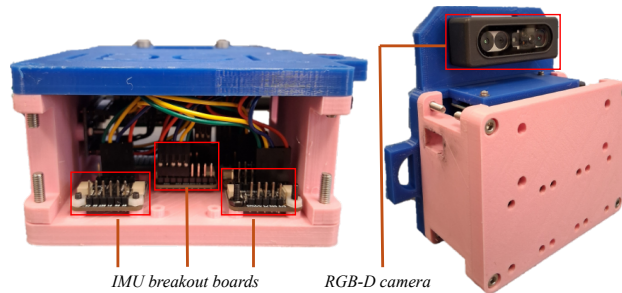


Fig. 2 Experimental platform showing front and side views with an RGB-D camera and three MEMS IMUs

Table 1 Estimated camera intrinsic parameters

Calibration parameter	Value (unit)
f_x	455.1313 (mm/pixels)
f_y	453.6879 (mm/pixels)
c_x	338.1614 (pixels)
c_y	241.9856 (pixels)
γ	-0.6977 (unitless)
λ_1	0.079 (unitless)
λ_2	-0.042 (unitless)
λ_3	-0.163 (unitless)
Mean reprojection error of checkerboard corners	0.20 (pixels)
Checkerboard images count	19

$R = TP/(TP + FN)$, $P = TP/(TP + FP)$, where TP , FP , FN denote true positives, false positives, and false negatives, respectively. In fact, precision is the fraction of predicted floor pixels that are actually floor pixels; this shows how accurate the positive predictions are. Recall is the fraction of actual floor pixels that were correctly identified. This shows how complete the detection is. These precision and recall values are measured at the pixel level. In order to achieve this, the pixels in the reference and segmented masks are compared to each other. The reference masks are acquired with the help of Grab-cut [49] algorithm as implemented in MATLAB. The recall and precision values of two test datasets are shown in Table 2. The results for local images (images taken from the same environment as the training set) show a high precision and recall value of 0.96. The standard deviation is small and in the range of 0.05 to 0.07 for these values. For the images taken from online databases, while the precision stays high (0.96), the recall value drops to 0.71. Further, the standard deviations increase significantly up to 0.23 for the precision and 0.31 for recall. This indicates that more images from diverse environments are required to increase the accuracy of the floor-segmentation. In order to depict the precision-recall curve, we change the binary threshold of foreground (floor) and background segmentation. The corresponding precision-recall values are shown in Figure 4.

The floor segment is back-projected to 3D space, where SVD-based plane fitting is achieved. The estimated plane normal is projected onto the image for visualization as shown in Figure 5 (shown as orange arrow). Red polygons show the convex hull of the points in the depth channel that are on the floor segment and used to estimate the normal.

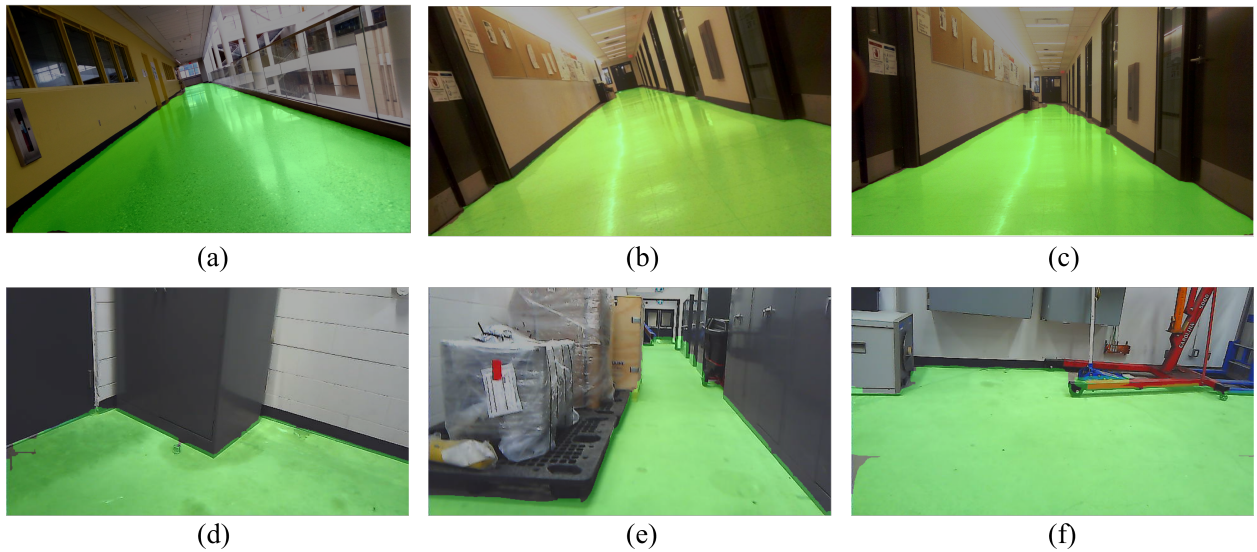
**Fig. 3 Floor detection results across different indoor environments (green: detected floor)**

Table 2 Performance comparison of tuned floor segmentation model (outcome of Module 1, Step 3)

Dataset	Number of Images	Mean Precision	Std. Precision	Mean Recall	Std. Recall
Local Images	31	0.96	0.05	0.96	0.07
Online Images	33	0.96	0.23	0.71	0.31

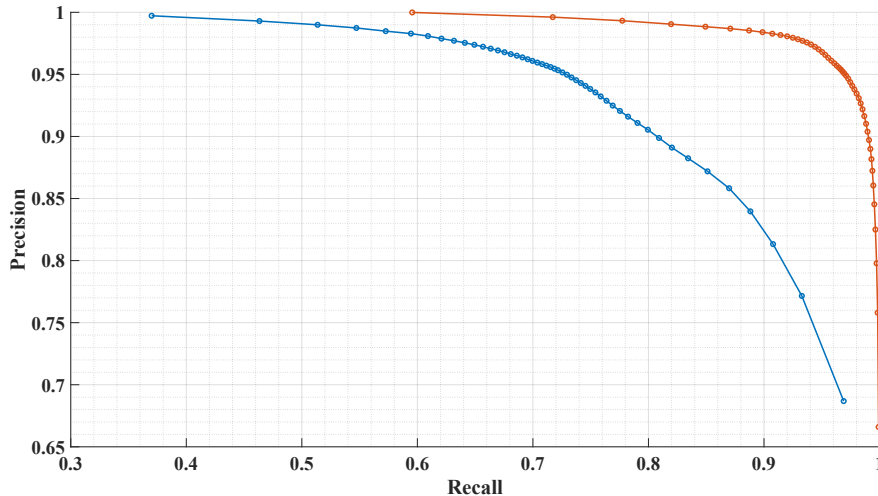


Fig. 4 Floor segmentation results: orange curve (same environment) and blue curve (online dataset)

After filtering the acceleration data in Module 2 Step 1, Step 2 involves static and dynamic phases that are necessary for estimating the intrinsic calibration parameters of the accelerometer. The detected dynamic phases are shown in Fig. 6 in purple. The intervals in between dynamic phases, in addition to the initial and the final phases, mark the static phases. For brevity, the static phases detection for only one of the IMUs, specifically ISM330DHCX, is provided.

The static/dynamic phases are utilized in Module 2, Step 3, to estimate the IMU intrinsic parameters. The final estimated values of these parameters are shown in Table 3. The parameters that have the highest influence are biases and scale factors, as they constitute the largest portion of the error. For an ideal IMU, the calibration parameters for the scale values should be 1 in all three axes, and should be zero for the bias. In the next section, the importance of calibration for the MPU6050 is discussed. Based on Table 3, MPU6050 exhibits much larger errors without calibration in both the scale and bias values, as this sensor belongs to an older generation of MEMS IMUs.

Table 3 Estimated intrinsic calibration parameters of the IMUs

Parameter	ISM330DHCX	MPU6050	LSM6DSOX
s_x	0.9940	1.1335	0.9957
n_{xy}	0.0186	0.3782	0.0081
s_y	1.0131	0.9200	0.9703
n_{xz}	-0.0070	0.3140	-0.0059
n_{yz}	-0.0159	-0.1310	0.0028
s_z	1.0023	0.9050	0.9997
b_x	0.0225	0.7308	-0.0128
b_y	0.0086	-0.5024	-0.0108
b_z	-0.1313	1.6950	-0.1189

In order to test the extrinsic calibration algorithm (Module 3), the images of the test dataset was not included in the floor segmentation training to correctly assess the generalizability of the trained neural nets to unseen scenes. The test set includes a variety of scenes. These include hallways, corners, and areas without any outstanding structures.

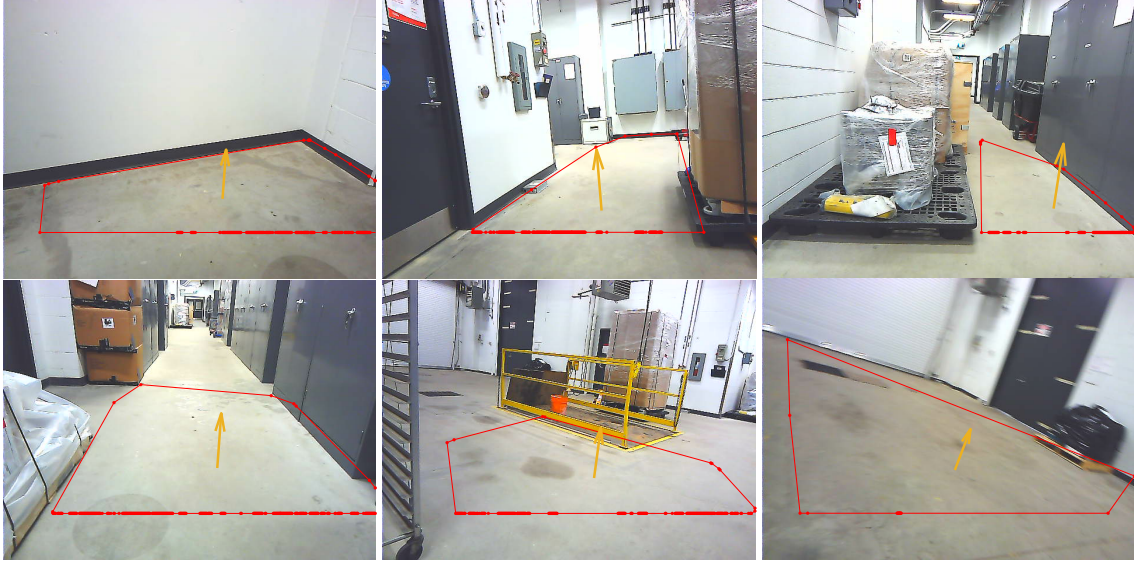


Fig. 5 Floor segmentation with surface normals in an industrial environment

The accuracy of the proposed extrinsic calibration algorithm is evaluated using MATLAB’s method [50] and Kalibr [2]. MATLAB’s RGB-D/IMU extrinsic calibration is a target-based method that requires a checkerboard. The method first estimates the trajectories of a camera and an IMU, independently and in a subsequent step, estimates the unknown extrinsic calibration parameters. While estimation of the camera’s trajectory with the help of a checkerboard can be achieved, such trajectory estimation for a low-cost MEMS IMU with 6 DoF does not provide a solution due to error accumulation. In order to address this challenge, the unknown extrinsic orientation parameters are calculated using the gyroscope measurement by modifying MATLAB’s RGB/IMU extrinsic calibration method. In this modification, the angular velocities of the camera are calculated using the estimated trajectory. With the help of estimated angular velocities in the camera’s frame and known gyroscope angular rate measurements in the IMU’s body frame, the extrinsic calibration parameters are estimated using a variety of solutions to Wahba’s problem. In particular, we have utilized the proposed RANSAC-based approach (as explained in Section II) as well as SVD [51], QUEST [52], and FLAE [53]. SVD-based solution to Wahba’s problem is an earlier approach, and it avoids representing the attitude with Euler or quaternion parameterizations; it directly estimates the rotation matrix. SVD is an alternative technique that is computationally expensive for real-time attitude estimation applications. Alternatively, QUEST utilizes quaternions and does not require a complete eigen vector decomposition, thus making it more suitable for online applications. FLAE is a non-iterative approach that also utilizes quaternions to estimate the attitude. The proposed method is further compared

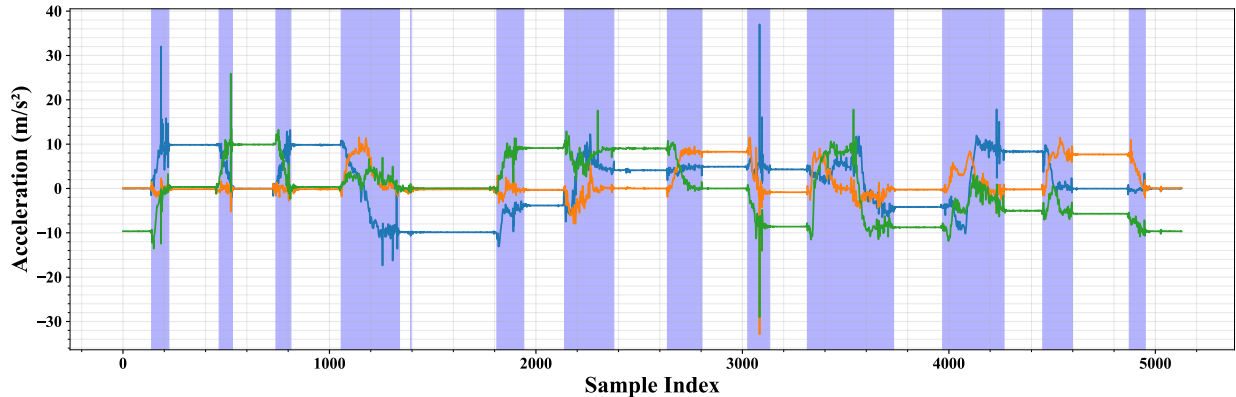


Fig. 6 Three-axis accelerometer data (ISM330DHCX) with detected dynamic phases in purple

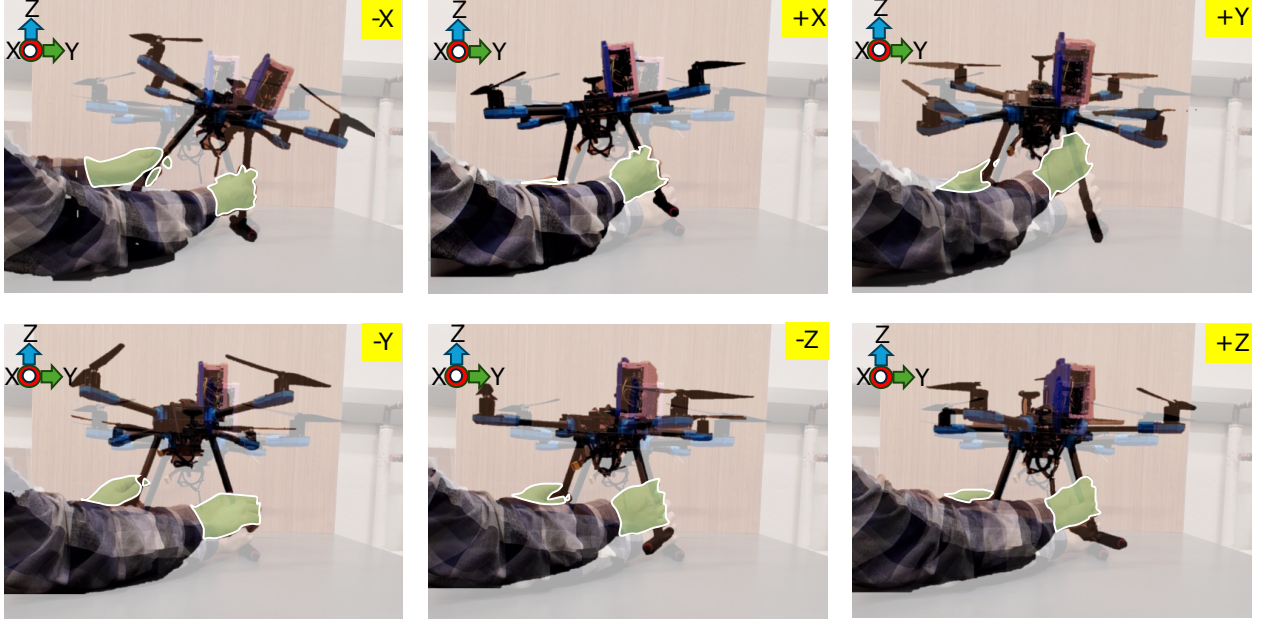


Fig. 7 The sequence of rotations in x , y , and z axes.

to Kablir [2]. Kalibr is a well-known target-based calibration technique of IMU and camera, relying on targets. Unlike MATLAB’s extrinsic calibration toolbox, Kalibr estimates the unknown extrinsic calibration while achieving sensor fusion during the motion of the sensors. This method is widely recognized as the standard approach to assessing the extrinsic calibration methods.

In order to measure the accuracy of the proposed method (Module 3), geodetic distance is utilized. The distance between two rotation matrices is calculated as

$$d(\mathbf{R}_{\text{Kalibr}}, \mathbf{R}_{\text{ref}}) = \cos^{-1} \left(\frac{\text{trace}(\mathbf{R}_{\text{Kalibr}}^T \mathbf{R}_{\text{ref}}) - 1}{2} \right). \quad (15)$$

To ensure that all extrinsic orientation parameters are observable, the three sensor axes must be excited during the data collection process. To achieve this, the sequence of motions shown in Figure 7 is performed. In this figure, the drone (with the IMU/RGB-D attached) is first rolled forward and backward, exciting motion along the x -axis. Next, the drone is pitched, producing rotation about the y -axis. Finally, the drone is rotated about the z -axis to generate yaw motion. During this motion, the floor segment should be in the field of view of the RGB-D camera.

We investigated the importance of Module 1, Step 1 on the accuracy of the extrinsic calibration. The extrinsic calibration accuracy is compared to KALIBR for cut-off frequency values of 0.5, 1, 2, 10, and 25 Hz for the three sensors, as shown in Fig. 8. The trials are repeated 50 times. The results in this plot indicate that, if other factors are held constant (such as intrinsic and extrinsic calibration), the filtering cut-off frequency has only a small effect on the final extrinsic calibration accuracy. In particular, for ISM330DHCX and LSM6DSOX, lower cut-off frequencies provide slightly better results in terms of average accuracy. However, for the MPU6050, a higher cut-off frequency of 20 Hz yields the best results. For the subsequent steps, only the best cut-off frequency values are selected for comparison.

Error comparison of robust methods for extrinsic orientation matrix estimation is shown in Table 4. In this table, the results for the RANSAC-based version of the proposed is shown. Due to larger number of outliers in the data, other robust attitude estimators, including FLAE, QUEST, could not estimate the attitude. However, for MATLAB’s checkerboard-based method, attitude estimation methods, RANSAC, SVD, QUEST, or FLAE, were able to estimate the calibration parameters and are included in this table. As we utilize different approaches to estimate the extrinsic orientation, given the trajectory from MATLAB’s Extrinsic Calibration Toolbox, the MATLAB–Wahba solver naming convention is used in Table 4, with the Wahba solver replaced by RANSAC, SVD, QUEST, or FLAE.

Table 4 illustrates the results with and without calibrating the accelerometer (Module 2, Step 3). Since RANSAC is a non-deterministic algorithm, the trials are repeated 50 times. The results of these 50 experiments are summarized as 25%, 50% and 75% quantiles. The methods such as SVD, QUEST, FLAE, and Kalibr are all deterministic methods, and

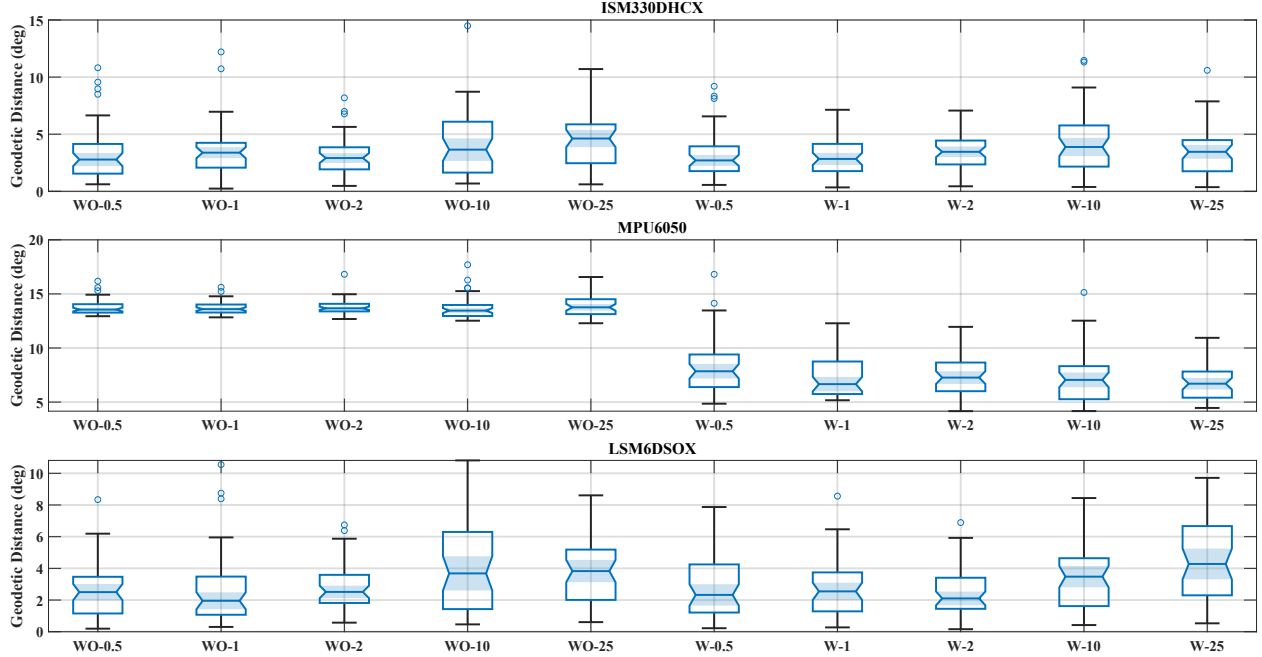


Fig. 8 Comparison of extrinsic calibration errors for RGB-D-IMU using different Butterworth filter cut-off frequencies

thus they achieve the same values for these quantiles across the experiment (the results are also graphically summarized in Fig. 9).

The results in Table 4 illustrate that the proposed method outperforms MATLAB's algorithm. Further, the intrinsic calibration of the IMU has reduced the errors with a total error 4.23° achieved using RANSAC and intrinsic calibration (proposed method with calibration). In fact, RANSAC was the only method that results in a successful extrinsic calibration using the proposed method.

Table 4 Error comparison of robust methods for extrinsic orientation matrix estimation

Method	Error in extrinsic rotation (degrees)									
	ISM330DHCX			MPU6050			LSM6DSOX			average
	25%	50%	75%	25%	50%	75%	25%	50%	75%	
proposed_RANSAC_WO	1.56	4.08	5.52	13.01	13.67	14.57	1.48	3.12	4.62	6.97
proposed_RANSAC_W	2.33	3.65	5.38	4.62	5.20	6.33	2.04	3.85	5.52	4.23
MATLAB_RANSAC	6.49	7.97	9.93	7.95	9.77	11.78	4.64	6.70	8.93	8.15
MATLAB_SVD	8.40	8.40	8.40	7.64	7.64	7.64	8.28	8.28	8.28	8.11
MATLAB_QUEST	8.43	8.43	8.43	7.35	7.35	7.35	8.94	8.94	8.94	8.24
MATLAB_FLAE	8.40	8.40	8.40	7.64	7.64	7.64	8.28	8.28	8.28	8.11
KALIBR	0.00	0.00	0.00	0.00	0.00	0.00	0.00	0.00	0.00	0.001

RANSAC parameters (such as outliers and the threshold for the distance) as shown in Algorithm 1 are summarized in Table 5. The number of points to fit a RANSAC model is kept as three. This is the minimum number of points required to estimate extrinsic orientation parameters with the help of the developed approach, as explained in Section II. The outlier rejection threshold is set to the values in Table 5 after trial and error. The detected inlier-to-outlier ratios are shown for each sensor in this table as well. As with the calibration parameters, it is expected to have a lower inlier to outlier ratio for MPU6050 as this sensor belongs to a relatively older generation compared to ISM330DHCX and LSM6DSOX.

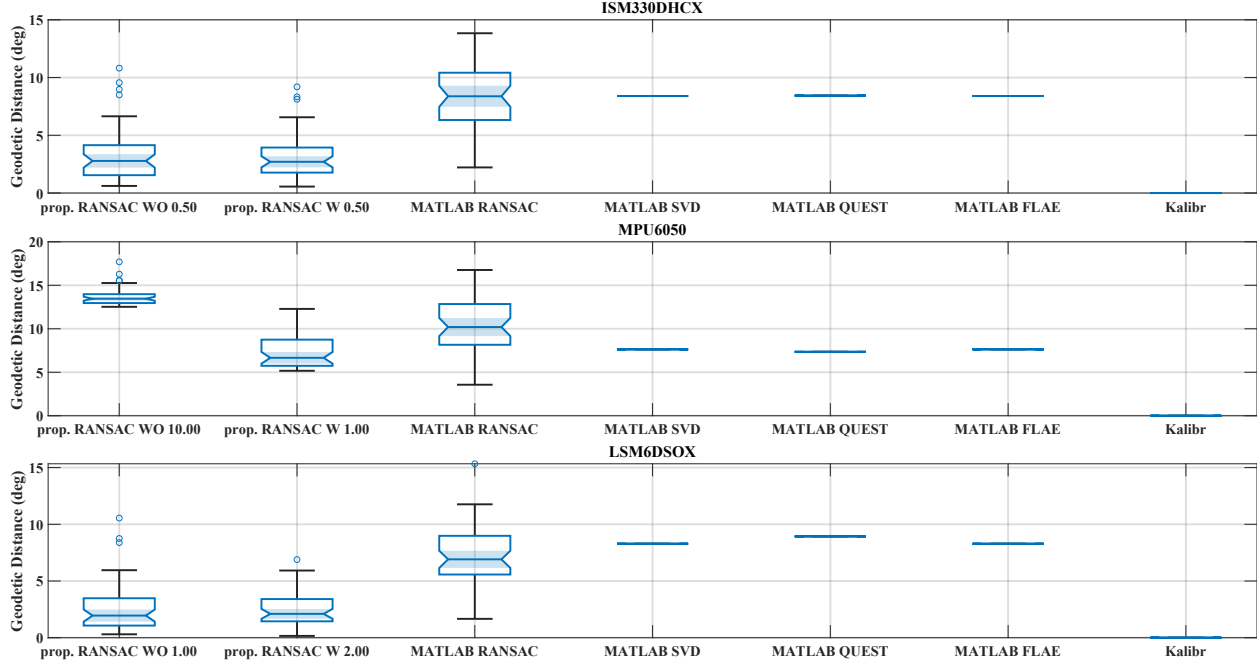


Fig. 9 Comparison of RGB-D-IMU extrinsic calibration errors: proposed method vs. MATLAB’s calibration

Table 5 Effect of threshold selection on proposed method performance

Configuration	ISM330DHCX	MPU6050	LSM6DSOX
model points = 3, outlier rejection threshold = 0.035	0.24	0.22	0.22
model points = 3, outlier rejection threshold = 0.3	0.31	0.22	0.32

IV. Conclusions and Future Work

In this study, we proposed a target-less approach to estimate the extrinsic calibration parameters of an IMU and an RGB-D camera with the help of a deep neural net-based floor-segmentation. The proposed method utilized segmentation to extract the pixels corresponding to the floor. The corresponding pixels in the depth image are utilized to estimate the floor-normal. This vector and the sensed gravity vector in the accelerometer’s frame are utilized to estimate the extrinsic calibration parameters using RANSAC.

The developed method is tested using Kalibr as the reference solution and MATLAB’s calibration techniques. Further, RANSAC-based estimation is compared to SVD, FLAE, and other robust estimators. The developed method is shown to be able to achieve a similar level of accuracy of the extrinsic calibration without relying on any targets. Further, it is shown that RANSAC-based estimation is most suitable for the developed approach due to its capacity to reject outliers in the data, while other methods, such as FLAE, failed. It is shown that intrinsic calibration of IMU’s plays a critical role in improving the overall accuracy.

The developed floor-segmentation is tested with two datasets. The precision of the developed method is reported to achieve approximately 96.0 precision and recall values for a test data set similar the training data set. For the outdoor environment, the mean precision value remains high, while the recall drops to approximately 71.0 percent. The developed floor-segmentation, however exhibits errors under low-illumination conditions and high levels of reflection on the floor and scenes. Thus, in the future, a model with wider applicability for the floor-segmentation can be developed.

One of the key limitations of the proposed method is that it assumes the floor normal vector is parallel to the gravity vector. Although this assumption is almost always valid in indoor, human-made environments, it often does not hold in outdoor environments. Furthermore, the proposed method cannot be applied if the floor segment is completely obscured by clutter. In the future, we plan to extend the proposed method to outdoor scenes. In particular, in cities with tall buildings (commonly referred to as the Manhattan World), the structural regularity can be leveraged to estimate the gravity direction from the camera, thereby enabling extrinsic calibration of the camera and IMU as well.

Funding Sources

This work was supported by the Natural Sciences and Engineering Research Council of Canada (NSERC), the Government of Alberta, Alberta Innovates, and the Schulich School of Engineering at the University of Calgary. Funding was awarded to Dr. Mahdis Bisheban, Director of the Intelligent Dynamics and Control Lab and Assistant Professor at the University of Calgary.

Code Availability

The source code and all calibration scripts used in this work are available at [RGBD2IMU_Calibration Github repository](#).

References

- [1] Ollero, A., Tognon, M., Suarez, A., Lee, D., and Franchi, A., “Past, present, and future of aerial robotic manipulators,” *IEEE Transactions on Robotics*, Vol. 38, No. 1, 2021, pp. 626–645.
- [2] Rehder, J., Nikolic, J., Schneider, T., Hinzmann, T., and Siegwart, R., “Extending Kalibr: Calibrating the Extrinsic of Multiple IMUs and of Individual Axes,” *Proceedings of the 2016 IEEE International Conference on Robotics and Automation (ICRA)*, IEEE, 2016, pp. 4304–4311. <https://doi.org/10.1109/ICRA.2016.7487580>.
- [3] Zhang, Y., Liang, W., Yuan, M., He, H., Tan, J., and Pang, Z., “Monocular Visual-Inertial and Robotic-Arm Calibration in a Unifying Framework,” *IEEE/CAA Journal of Automatica Sinica*, Vol. 9, No. 1, 2021, pp. 146–159.
- [4] Qin, T., Li, P., and Shen, S., “VINS-Mono: A Robust and Versatile Monocular Visual-Inertial State Estimator,” *IEEE Transactions on Robotics*, Vol. 34, No. 4, 2018, pp. 1004–1020.
- [5] Huang, W., Liu, H., and Wan, W., “An Online Initialization and Self-Calibration Method for Stereo Visual-Inertial Odometry,” *IEEE Transactions on Robotics*, Vol. 36, No. 4, 2020, pp. 1153–1170. <https://doi.org/10.1109/TRO.2019.2959161>.
- [6] Huai, J., Lin, Y., Zhuang, Y., Toth, C. K., and Chen, D., “Observability Analysis and Keyframe-Based Filtering for Visual Inertial Odometry with Full Self-Calibration,” *IEEE Transactions on Robotics*, Vol. 38, No. 5, 2022, pp. 3219–3237.
- [7] Wang, Z., and Cheng, X., “Adaptive Optimization Online IMU Self-Calibration Method for Visual-Inertial Navigation Systems,” *Measurement*, Vol. 180, 2021.
- [8] Lee, J., Hanley, D., and Bretl, T., “Extrinsic calibration of multiple inertial sensors from arbitrary trajectories,” *IEEE Robotics and Automation Letters*, Vol. 7, No. 2, 2022, pp. 2055–2062.
- [9] Ouyang, W., Lin, W., and Sun, L., “A dynamic and static combined camera-IMU extrinsic calibration method based on continuous-time trajectory estimation,” *Robotics and Autonomous Systems*, Vol. 186, 2025, p. 104916.
- [10] Yang, Z., and Shen, S., “Monocular visual-inertial state estimation with online initialization and camera-IMU extrinsic calibration,” *IEEE Transactions on Automation Science and Engineering*, Vol. 14, No. 1, 2016, pp. 39–51.
- [11] Nistér, D., “An efficient solution to the five-point relative pose problem,” *IEEE transactions on pattern analysis and machine intelligence*, Vol. 26, No. 6, 2004, pp. 756–770.
- [12] Xiao, J., Guo, J., Ouyang, C., Shi, J., Xu, Y., and Wu, M., “A Slope-Based Targetless Extrinsic Calibration Method for LiDAR-IMU Systems on Ground Vehicles,” *IEEE Transactions on Instrumentation and Measurement*, 2025.
- [13] Kitt, B. M., Rehder, J., Chambers, A. D., Schonbein, M., Lategahn, H., and Singh, S., “Monocular Visual Odometry using a Planar Road Model to Solve Scale Ambiguity,” *Proceedings of 5th European Conference on Mobile Robots (ECMR ’11)*, 2011, pp. 43 – 48.
- [14] Zhou, D., Dai, Y., and Li, H., “Ground-plane-based absolute scale estimation for monocular visual odometry,” *IEEE Transactions on Intelligent Transportation Systems*, Vol. 21, No. 2, 2019, pp. 791–802.
- [15] Wei, D., Ran, H., Li, Z., and Gao, T., “Enhanced low drift LiDAR SLAM with dynamic noise using ground principal plane constraint,” *Measurement*, Vol. 245, 2025, p. 116549.
- [16] Kim, T., Pak, G., and Kim, E., “GRIL-Calib: targetless ground robot IMU-LiDAR extrinsic calibration method using ground plane motion constraints,” *IEEE Robotics and Automation Letters*, Vol. 9, No. 6, 2024, pp. 5409–5416.

- [17] Ai, M., Hokmabadi, I. A. S., Elhabiby, M., Moussa, M., Zekry, A., Mohamed, A., and El-Sheimy, N., "Lidar-Inertial Localization with Ground Constraint in a Point Cloud Map," ISPRS Annals of the Photogrammetry, Remote Sensing and Spatial Information Sciences, Vol. X, 2023, pp. 613–619.
- [18] Li, W., Wang, G., Zhang, Q., and Liu, J., "LG-VIWO: Visual-Inertial-Wheel Odometry Leveraging the Depth-aided Local Ground Constraints for Mobile Robots," IEEE Transactions on Instrumentation and Measurement, 2025.
- [19] Pritzl, V., Vrba, M., Tortorici, C., Ashour, R., and Saska, M., "Adaptive Estimation of UAV Altitude in Complex Indoor Environments Using Degraded and Time-Delayed Measurements with Time-Varying Uncertainties," Robotics and Autonomous Systems, Vol. 160, 2023. <https://doi.org/10.1016/j.robot.2022.104281>.
- [20] Zhao, L., Wang, W., He, Q., Yan, L., and Li, X., "Visual-Inertial Autonomous UAV Navigation in Complex Illumination and Highly Cluttered Under-Canopy Environments," Drones, Vol. 9, No. 1, 2025. <https://doi.org/10.3390/drones9010001>.
- [21] Whitney, E., Gopu, B. P. R., and Tiwari, M., "3D Global Localization of a UAV Using 2D Monte Carlo Localization and Ground Plane Extraction," AIAA SCITECH 2025 Forum, 2025.
- [22] Chen, J., Zhang, Y., Li, J., Du, W., Chen, Z., Liu, Z., Wang, H., and Leung, V. C., "Integrated air-ground vehicles for UAV emergency landing based on graph convolution network," IEEE Internet of Things Journal, Vol. 9, No. 12, 2021, pp. 9106–9116.
- [23] Berenguel-Baeta, B., Guerrero-Viu, M., Nova, A., Bermudez-Cameo, J., Pérez-Yus, A., and Guerrero, J. J., "Floor extraction and door detection for visually impaired guidance," 2020 16th International Conference on Control, Automation, Robotics and Vision (ICARCV), IEEE, 2020, pp. 1222–1229.
- [24] Tian, R., Zhang, Y., Zhu, D., Liang, S., Coleman, S., and Kerr, D., "Accurate and robust scale recovery for monocular visual odometry based on plane geometry," 2021 IEEE International Conference on Robotics and Automation (ICRA), IEEE, 2021, pp. 5296–5302.
- [25] Gomes, T., Matias, D., Campos, A., Cunha, L., and Roriz, R., "A survey on ground segmentation methods for automotive LiDAR sensors," Sensors, Vol. 23, No. 2, 2023, p. 601.
- [26] Liu, D., Ni, H., Zhou, X., Yang, N., and Yan, W., "Flexible ground constrained LiDAR SLAM with a novel plane detection," Computers and Electrical Engineering, Vol. 117, 2024, p. 109287.
- [27] Lowe, D. G., "Distinctive image features from scale-invariant keypoints," International journal of computer vision, Vol. 60, No. 2, 2004, pp. 91–110.
- [28] Man, Y., Weng, X., Li, X., and Kitani, K., "GroundNet: Monocular ground plane normal estimation with geometric consistency," Proceedings of the 27th ACM International Conference on Multimedia, 2019, pp. 2170–2178.
- [29] Hamandi, M., Asmar, D., and Shamma, E., "Ground segmentation and free space estimation in off-road terrain," Pattern Recognition Letters, Vol. 108, 2018, pp. 1–7.
- [30] Paigwar, A., Erkent, Ö., Sierra-Gonzalez, D., and Laugier, C., "GndNet: Fast ground plane estimation and point cloud segmentation for autonomous vehicles," 2020 IEEE/RSJ international conference on intelligent robots and systems (IROS), IEEE, 2020, pp. 2150–2156.
- [31] Duda, R. O., and Hart, P. E., "Use of the Hough transformation to detect lines and curves in pictures," Communications of the ACM, Vol. 15, No. 1, 1972, pp. 11–15.
- [32] Li, Y., and Gan, X., "An integrated fast Hough transform for multidimensional data," IEEE transactions on pattern analysis and machine intelligence, Vol. 45, No. 9, 2023, pp. 11365–11373.
- [33] Schubert, E., Sander, J., Ester, M., Kriegel, H. P., and Xu, X., "DBSCAN revisited, revisited: why and how you should (still) use DBSCAN," ACM Transactions on Database Systems (TODS), Vol. 42, No. 3, 2017, pp. 1–21.
- [34] Martínez-Otzeta, J. M., Rodríguez-Moreno, I., Mendiáldua, I., and Sierra, B., "Ransac for Robotic Applications: A Survey," Sensors, Vol. 23, 2022.
- [35] Li, L., Yang, F., Zhu, H., Li, D., Li, Y., and Tang, L., "An improved RANSAC for 3D point cloud plane segmentation based on normal distribution transformation cells," Remote Sensing, Vol. 9, No. 5, 2017, p. 433.
- [36] Zhang, Z., "Flexible camera calibration by viewing a plane from unknown orientations," Proceedings of the seventh IEEE international conference on computer vision, Vol. 1, IEEE, 1999, pp. 666–673.

- [37] The MathWorks, I., “Camera Calibration,” 2025. URL <https://www.mathworks.com/help/vision/camera-calibration.html>, accessed: August 25, 2025.
- [38] Tedaldi, D., Pretto, A., and Menegatti, E., “A robust and easy to implement method for IMU calibration without external equipments,” 2014 IEEE international conference on robotics and automation (ICRA), IEEE, 2014, pp. 3042–3049.
- [39] Khankalantary, S., Ranjbaran, S., and Ebadollahi, S., “Simplification of Calibration of Low-Cost MEMS Accelerometer and Its Temperature Compensation Without Accurate Laboratory Equipment,” Measurement Science and Technology, Vol. 32, 2021. <https://doi.org/10.1088/1361-6501/abd0bf>.
- [40] Wang, Z., Chaoyang, X., and Liheng, C., “A Calibration Method of g-sensitivity Error of MEMS Gyroscope,” International Conference on Autonomous Unmanned Systems, Springer Singapore, 2021, pp. 1957–1965.
- [41] Qureshi, U., and Golnaraghi, F., “An Algorithm for the In-Field Calibration of a MEMS IMU,” IEEE Sensors Journal, Vol. 17, 2017. <https://doi.org/10.1109/JSEN.2017.2751572>.
- [42] Wahba, G., “A least squares estimate of satellite attitude,” SIAM review, Vol. 7, No. 3, 1965, pp. 409–409.
- [43] Wu, J., Zhou, Z., Fourati, H., and Liu, M., “Lasso Wahba’s Problem and Its Analytical Solution for Spacecraft Attitude Determination,” 2021 IEEE 17th International Conference on Automation Science and Engineering (CASE), IEEE, 2021, pp. 1040–1046. <https://doi.org/10.1109/CASE49439.2021.9551389>.
- [44] Chen, B., Lin, Y., Chen, J., Huang, C., Chern, J., and Sun, C., “FracGM: A Fast Fractional Programming Technique for Geman-McClure Robust Estimator,” IEEE Robotics and Automation Letters, Vol. 9, No. 12, 2024, pp. 11666–11673. <https://doi.org/10.1109/LRA.2024.3495372>.
- [45] Orbbec Technology (Shenzhen) Co., Ltd., “Gemini 2 3D Camera (Active Stereo IR Depth Sensor),” <https://www.orbbec.com/products/stereo-vision-camera/gemini-2/>, 2023. Accessed: 2025-08-19.
- [46] Adafruit, “ISM330DHCX 6-DOF IMU Breakout,” <https://www.adafruit.com/product/4502>, n.d.. Accessed: 2025-08-19.
- [47] Adafruit, “LSM6DSOX 6-DOF IMU Breakout,” <https://www.adafruit.com/product/4438>, n.d.. Accessed: 2025-08-19.
- [48] TDK InvenSense, MPU-6050 6-DOF IMU Breakout, TDK InvenSense, rev. 3.4 ed., August 2013. URL <https://invensense.tdk.com/wp-content/uploads/2015/02/MPU-6000-Datasheet1.pdf>, accessed: 2025-08-19.
- [49] Rother, C., Kolmogorov, V., and Blake, A., ““GrabCut”: interactive foreground extraction using iterated graph cuts,” ACM Trans. Graph., Vol. 23, No. 3, 2004, p. 309–314. <https://doi.org/10.1145/1015706.1015720>, URL <https://doi.org/10.1145/1015706.1015720>.
- [50] MathWorks, “Estimate Camera-to-IMU Transformation Using Extrinsic Calibration,” <https://www.mathworks.com/help/nav/ug/estimate-camera-to-imu-transformation-using-extrinsic-calibration.html>, 2025. Accessed: 2025-08-19.
- [51] Farrell, J., Stuelpnagel, J., Wessner, R., Velman, J., and Brook, J., “A least squares estimate of satellite attitude (Grace Wahba),” SIAM review, Vol. 8, No. 3, 1966, pp. 384–386.
- [52] Cheng, Y., and Shuster, M. D., “Improvement to the Implementation of the QUEST Algorithm,” Journal of Guidance, Control, and Dynamics, Vol. 37, No. 1, 2014.
- [53] Wu, J., Zhou, Z., Gao, B., Li, R., Cheng, Y., and Fourati, H., “Fast Linear Quaternion Attitude Estimator Using Vector Observations,” IEEE Transactions on Automation Science and Engineering, Vol. 15, 2017.